Scientific Research Publishing

Materials Sciences and Applications, 2019, 10, 631-642
https://www.scirp.org/journal/msa
ISSN Online: 2153-1188
ISSN Print: 2153-117X

Temperature-Programmed Reduction and Dispersive X-Ray Absorption Spectroscopy Studies of CeO_2-Based Nanopowders for Intermediate-Temperature Solid-Oxide Fuel Cell Anodes

Marina S. Bellora[1,2], Joaquín Sacanell[2,3*], Cristián Huck-Iriart[1], Analía L. Soldati[3], Susana A. Larrondo[4,5], Diego G. Lamas[1]

[1]CONICET/Laboratorio de Cristalografía Aplicada, Escuela de Ciencia y Tecnología, Universidad Nacional de General San Martín, San Martín, Argentina
[2]Departamento de Física de la Materia Condensada, Gerencia de Investigación y Aplicaciones, Centro Atómico Constituyentes, Comisión Nacional de Energía Atómica, San Martín, Argentina
[3]Instituto de Nanociencia y Nanotecnología (INN), CNEA-CONICET, San Martín and San Carlos de Bariloche, Argentina
[4]UNIDEF-CONICET-MINDEF, Departamento de Investigaciones en Sólidos, CITEDEF, Villa Martelli, Argentina
[5]Instituto de Investigación e Ingeniería Ambiental, Universidad Nacional de General San Martín, San Martín, Argentina
Email: *sacanell@tandar.cnea.gov.ar

How to cite this paper: Bellora, M.S., Sacanell, J., Huck-Iriart, C., Soldati, A.L., Larrondo, S.A. and Lamas, D.G. (2019) Temperature-Programmed Reduction and Dispersive X-Ray Absorption Spectroscopy Studies of CeO_2-Based Nanopowders for Intermediate-Temperature Solid-Oxide Fuel Cell Anodes. *Materials Sciences and Applications*, **10**, 631-642.
https://doi.org/10.4236/msa.2019.1010045

Received: September 2, 2019
Accepted: October 14, 2019
Published: October 17, 2019

Abstract

In this work, we study the influence of the average crystallite size and dopant oxide on the reducibility of CeO_2-based nanomaterials. Samples were prepared from commercial Gd_2O_3-, Sm_2O_3- and Y_2O_3-doped CeO_2 powders by calcination at different temperatures ranging between 400˚C and 900˚C and characterized by X-ray powder diffraction, transmission electron microscopy and BET specific surface area. The reducibility of the samples was analyzed by temperature-programmed reduction and *in situ* dispersive X-ray absorption spectroscopy techniques. Our results clearly demonstrate that samples treated at lower temperatures, of smallest average crystallite size and highest specific surface areas, exhibit the best performance, while Gd_2O_3-doped ceria materials display higher reducibility than Sm_2O_3- and Y_2O_3-doped CeO_2.

Keywords

Crystallite Size, CeO_2-Based Nanomaterials, Sm_2O_3

1. Introduction

Cerium oxide (CeO_2) has been studied for many years and it is still the focus of

great attention due its wide range of possible applications. It is used in three-way catalysts (TWCs) for the elimination of toxic auto-exhaust gases [1] [2] low-temperature water-gas shift (WGS) reaction [3] [4], oxygen sensors [5] [6], oxygen permeation membrane systems [7] [8] and solid-oxide fuel cells (SOFCs) [9] [10] [11] [12], among others.

In all the aforementioned applications, there is a growing interest in the study of nanostructured materials, in which an improved surface-to-volume ratio can be obtained. This interest is founded in the consequent substantial reduction in the energy for defect formation occurs in nanocrystalline CeO_2, that leads to a high degree of non-stoichiometry and electronic carrier generation [13] both beneficial for redox, catalytic and transport properties. For example, CeO_2-based nanoceramics exhibit enhanced ionic conductivity [14], which is very important for their application as SOFC electrolytes.

Although the benefit of the use of nanostructured materials has already been pointed out by several authors, the studies of this type of materials from the basic point of view to understand the mechanisms underlying the different processes of catalysis are scarce. In recent years, our research groups have investigated CeO_2-based and NiO/CeO_2-based catalysts by dispersive X-ray absorption spectroscopy (DXAS) under different atmospheres and reaction conditions [15] [16] [17] [18]. Samples with different morphologies were analyzed, finding that CeO_2-based materials with small average crystallite size and high specific surface area exhibit the best properties, reaching high reducibility and excellent methane conversion for intermediate temperatures [19].

In this work, we analyzed the redox behavior of nanocrystalline Gd_2O_3, Sm_2O_3 and Y_2O_3-doped CeO_2 (GDC, SDC and YDC, respectively) powders. We used conventional laboratory temperature programmed reduction (TPR) and combined those results with an *in-situ* DXAS study under diluted hydrogen atmosphere, in order to gain further insight on the redox properties of the systems. The samples were treated at different temperatures, between 400˚C and 900˚C to analyze the influence of the crystallite size.

2. Experimental Procedure

Samples were prepared from nanocrystalline commercial (Nextech Materials) $Ce_{0.8}Gd_{0.2}O_{1.9}$ (GDC), CeO_2-10 mol% Sm_2O_3 ($Ce_{0.82}Sm_{0.18}O_{1.91}$, SDC) and CeO_2-10 mol% Y_2O_3 ($Ce_{0.82}Y_{0.18}O_{1.91}$, YDC) powders. They were calcined at 400˚C, 650˚C and 900˚C in order to study the influence of the average crystallite size.

X-ray powder diffraction (XPD) was performed in a Brucker D8 Discover DaVinci diffractometer (Institute of Physics, University of Sao Paulo, Brazil) operated with Cu-Kα radiation at 40 kV and 30 mA, a Ni filter and a Lynx-eye detector, in Bragg-Brentano configuration. Experimental data were collected in the angular 2θ range of 20˚ - 140˚ with a step size of 0.02˚ and a time per step of 1 s. The average crystallite sizes of the crystalline phases were determined for all the samples using the Scherrer equation.

Specific surface area was evaluated by means of N_2-physisorption with a Quantachrome Corporation Autosorb-1 equipment. Samples were previously degassed with pure He at 90˚C during 12 h. Results were obtained using the five-point Brunauer-Emmett-Teller (BET) method.

Transmission Electron Microscopy (TEM) experiments were performed using a Philips CM 200 UT microscope operated at 200 kV. The microscope was equipped with ultratwin objective lens and an EDAX spectrometer for chemical analysis by EDS. Powdered samples were suspended in isopropyl alcohol, ultrasonicated for 2 minutes and deposited in Cu/ultrathin hollow carbon TEM grids (Ted Pella).

Hydrogen temperature programmed reduction (TPR) experiments were performed in a Micromeritics Chemisorb 2720 equipment to study sample reducibility. The mass employed for each experiment was of 80 mg. Prior to TPR tests, samples were pretreated in He at 300˚C during 30 min to remove any adsorbed species on the solid surface. TPR was carried out with a 50 cm^3 (STP) min^{-1} (5 vol.% H_2/Ar) flow from room temperature up to 800˚C following a heating ramp of 10˚C min^{-1}. Hydrogen uptake was estimated using a Thermal Conductivity Detector (TCD) previously calibrated.

Dispersive X-ray absorption spectroscopy (DAXS) study was performed at the D06A-DXAS dispersive beamline of the Brazilian Synchrotron Light Laboratory (LNLS, Campinas, Brazil). A Si (111) monochromator was used altogether with a CCD detector to collect the absorption spectrum in transmission mode. Self-supporting discs were prepared by mixing the sample powder with boron nitride that has no significant absorption in the energy ranges used. The catalyst mass in the discs was calculated in order to obtain a total absorption ratio of 1.5. Sample discs were located in a sample-holder with a thermocouple attached to it. The sample holder was placed in a quartz reactor, with inlet and outlet gas lines, and located in a furnace with temperature control. Inlet gas composition was set with a gas-mixing station provided with mass flow controllers and exit composition was assessed with a Pfeiffer Omnistar mass spectrometer.

We followed the evolution of DXAS spectra as function of temperature at the L_3-edge of Ce under diluted H_2(5% in He), in order to determine the Ce^{3+}/Ce^{4+} proportion. The temperature range was of 400˚C - 800˚C. CeO_2 and $Ce(NO_3)_3{\cdot}6H_2O$ were also measured as standards. Ce^{3+}/Ce^{4+} proportion was obtained by means of linear least square procedures using Python scripting.

3. Results and Discussion

X-ray diffraction patterns for the samples calcined at 400˚C are presented in Figure 1. All of them display the expected fluorite-type crystal structure with no sign of any impurity. The nanostructured character of the powders is evidenced by their wide Bragg peaks.

Samples of the three compounds were treated at different temperatures, in order to obtain powders with different particle sizes. Figure 2 displays the X-ray

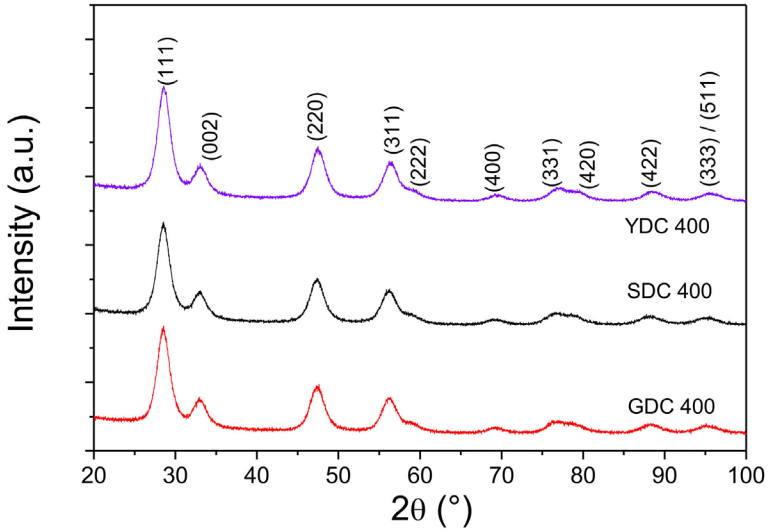

Figure 1. X-ray diffraction patterns for all compounds treated at 400˚C.

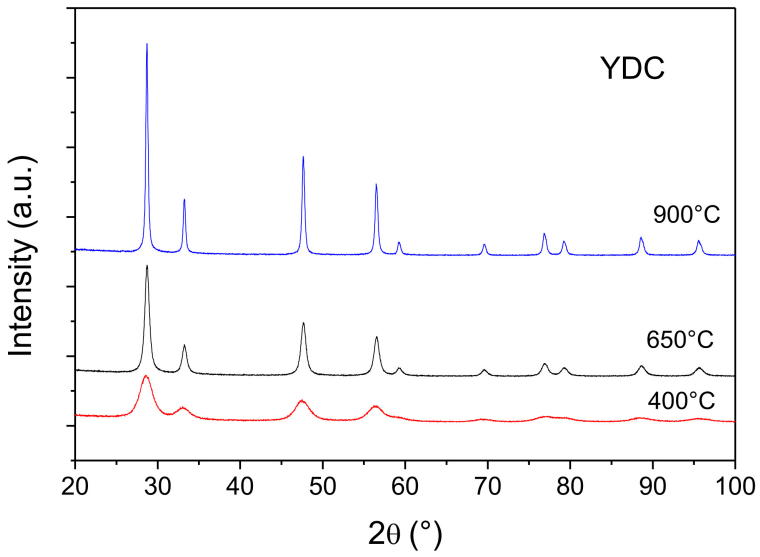

Figure 2. X-ray diffraction patterns for YDC powders compounds treated at 400˚C, 650˚C and 900˚C.

diffraction patterns for YDC nanopowders treated at 400˚C, 650˚C and 900˚C. As expected, the broadening of Bragg peaks decreases for increasing calcination temperature because samples treated at higher temperatures are formed by larger crystallites. The average crystallite sizes (D) determined from the Scherrer equation for all samples are summarized in **Table 1**. Crystallite sizes range from around 5 to ~50 nm. In particular, the SDC sample treated at 900˚C, is formed by crystallite significantly larger than GDC and YDC samples calcined at the same temperature.

Figure 3 displays selected TEM images taken from several samples treated at 650˚C. From those images, it can be observed that particle sizes are of the same order of magnitude of crystallite sizes (**Table 1**), thus indicating that particles

Table 1. Average crystallite size in nm determined using Scherrer equation for all the samples studied in this work.

Sample	400˚C	650˚C	900˚C
GDC	4.5(2)	14(1)	36(3)
SDC	4.6(2)	13(1)	48(4)
YDC	4.6(2)	14(1)	36(3)

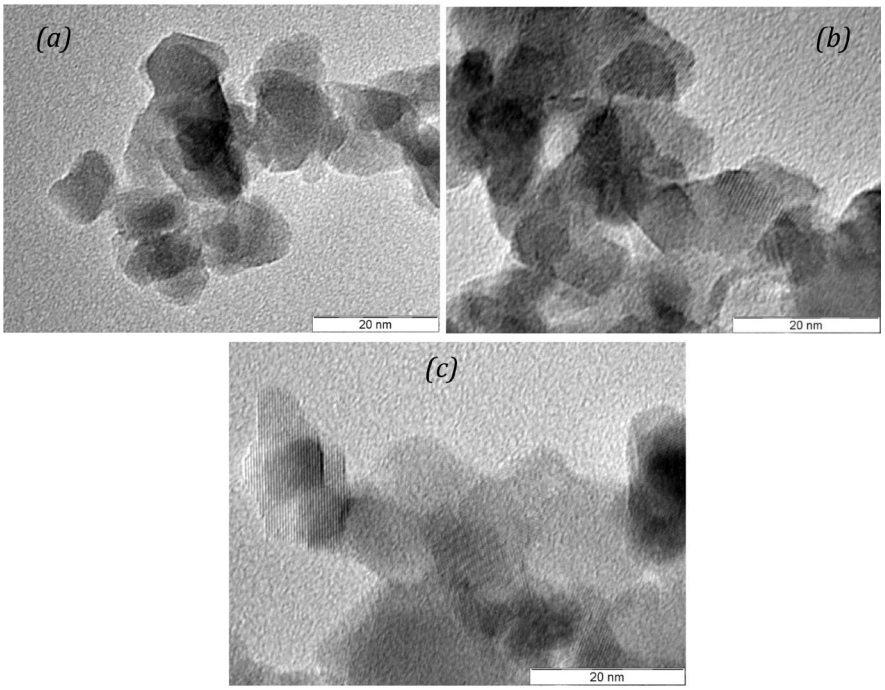

Figure 3. TEM images of the samples calcined at 650˚C: (a) GDC, (b) SDC, (c) YDC.

are single crystals. This feature was also observed for samples treated at 400˚C and for samples treated at 900˚C, as exemplified in **Figure 4** for the SDC system. From the morphological point of view, it can be seen that the particles display polygonal shapes in samples treated at higher temperatures.

The dependence of the average crystallite size as a function of calcination temperature is presented in **Figure 5**, where it can be seen that crystallite growth is less significant in GDC and YDC compared to SDC. In any case, in undoped ceria the effect is more prominent than that observed in the present work [20] [21]. This is a consequence of the inhibition produced by the solute drag model due to a space charge effect [22]. Y_2O_3 is known as one of the most efficient inhibitors of grain boundary mobility [20], here we show that Gd_2O_3 has a very similar effect.

The values of BET specific surface area of the samples are summarized in **Table 2**. As it can be observed in **Figure 5**, there is a marked correlation between SSA and average crystallite size, showing inverse trends for increasing calcination temperature.

The temperature-programmed reduction (TPR) profiles of samples calcined at

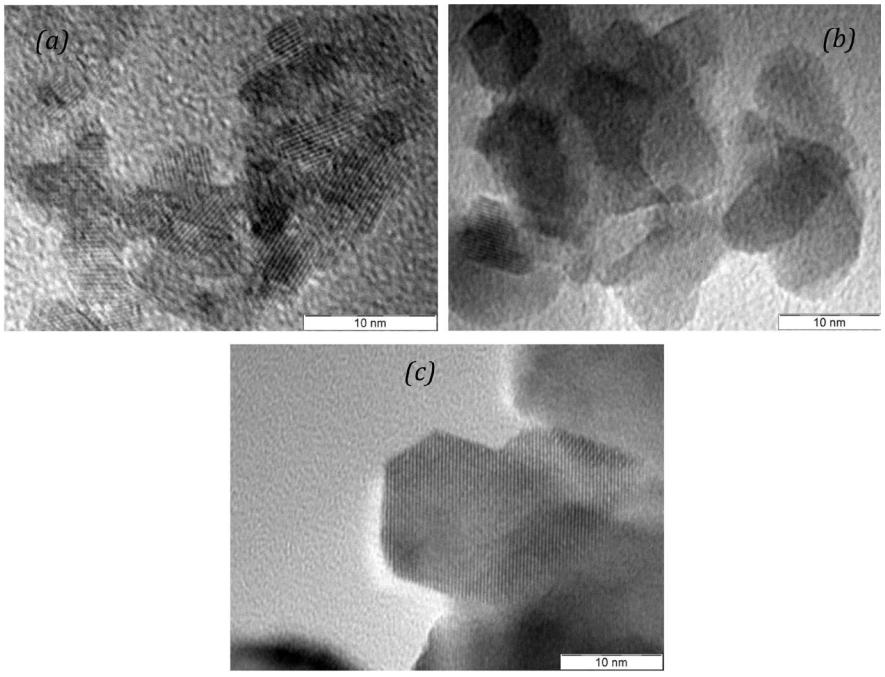

Figure 4. TEM images for the SDC samples treated at (a) 400˚C, (b) 650˚C, (c) 900˚C.

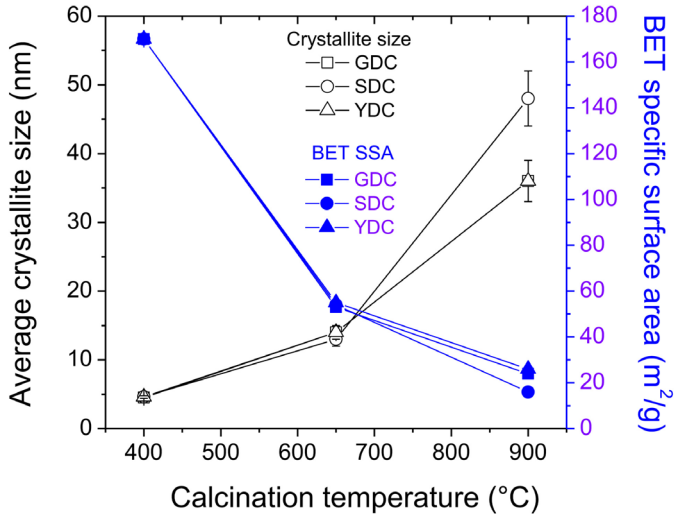

Figure 5. Average crystallite size and BET specific surface area as functions of calcination temperature.

Table 2. BET specific surface area in m^2/g for all samples.

Sample	400˚C	650˚C	900˚C
GDC	170	53	24
SDC	170	54	16
YDC	170	55	26

650˚C are shown in **Figure 6**. The TPR signal, directly related with hydrogen consumption, is presented as a function of the temperature of the sample. The

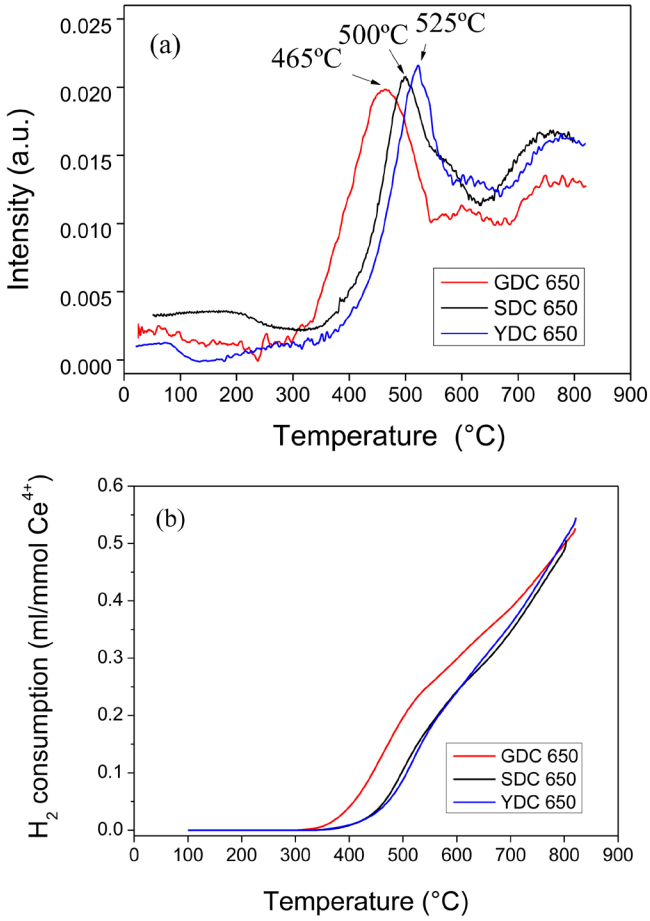

Figure 6. (a) TPR profile and (b) hydrogen consumption, for samples calcined at 650˚C.

curves do not present the same shape, position and height of the maximum. It is clearly observed that the main peak for all samples is close to 500˚C, while a secondary peak is detected around 770˚C. The main peak corresponding to the GDC sample, notably occurs at a lower temperature than those corresponding to YDC and SDC, indicating that the first is more efficient for hydrogen oxidation than the other two. Besides, SDC sample is slightly better than YDC one considering their reducibility, in view of the lower temperature at which hydrogen consumption is triggered. No significant difference is observed between the secondary peak of the three samples. The same trend was observed for samples treated at 400˚C and 900˚C. In **Figure 6(b)** we show the hydrogen consumption as a function of temperature in which the overall picture is clarified. Indeed, hydrogen consumption of GDC triggers at significantly lower temperature and is higher in the whole temperature range, than that corresponding to SDC and YDC, which are both very similar.

We also studied the influence of the average crystallite size on the reducibility of the samples. **Figure 7(a)** displays the TPR profiles for the YDC system as an example. It can be observed that the temperature of the main peak decreases with increasing calcination temperature, thus indicating that samples of lower

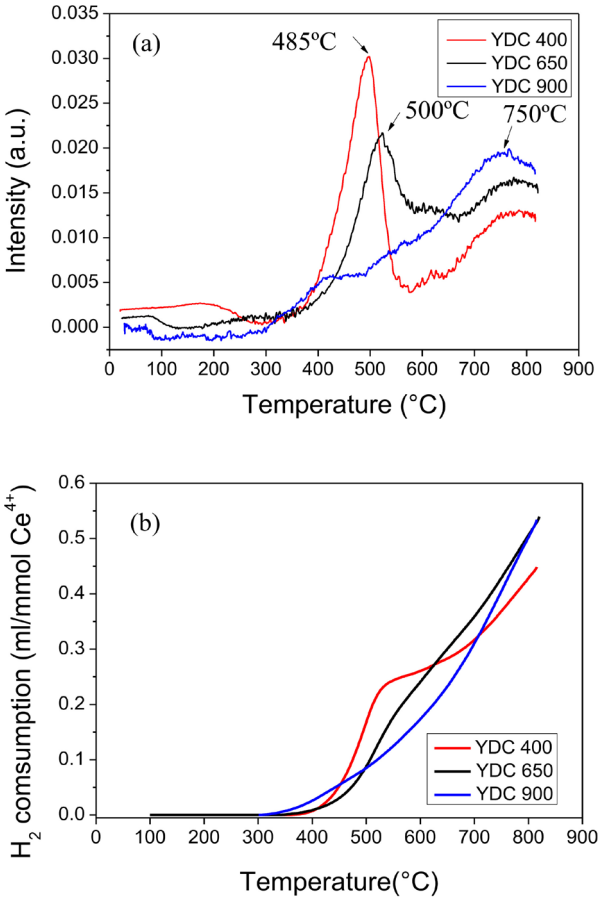

Figure 7. (a) TPR profiles and (b) hydrogen consumption for YDC samples.

average crystallite size are more efficient than those with larger particles. The same overall trend is observed for the other two systems (not shown). Regarding hydrogen consumption (**Figure 7(b)**), it can be noticed that it is enhanced in the sample treated at 400˚C, confirming again the enhanced reducibility of samples with smallest crystallites.

The above results regarding the influence of crystallite size and dopant oxide on the reducibility of the samples were further confirmed by using the DXAS technique under diluted H_2 atmosphere (5 mol% H_2/He). The experimental procedure was designed in order to mimic the conditions of the laboratory TPR experiments. For example, DXAS data taken at the Ce L_3-edge for the SDC nanopowder calcined at 400˚C is shown in **Figure 8**, displaying the evolution as a function of temperature. At room temperature, two peaks characteristic of Ce^{4+} are detected, while one peak corresponding to Ce^{3+} becomes more prominent at high temperatures. By measuring DXAS data corresponding to Ce^{3+} and Ce^{4+} standards and using a linear combination procedure, it was possible to determine the Ce^{3+} fraction as a function of temperature for all the samples.

Figure 9 displays the Ce^{3+} fraction ($\alpha_{Ce}{}^{3+}$) as a function of temperature for GDC, SDC and YDC samples treated at 400˚C (**Figure 8(a)**) and 650˚C (**Figure 8(b)**). As it can be observed that the largest values of $\alpha_{Ce}{}^{3+}$ were exhibited by

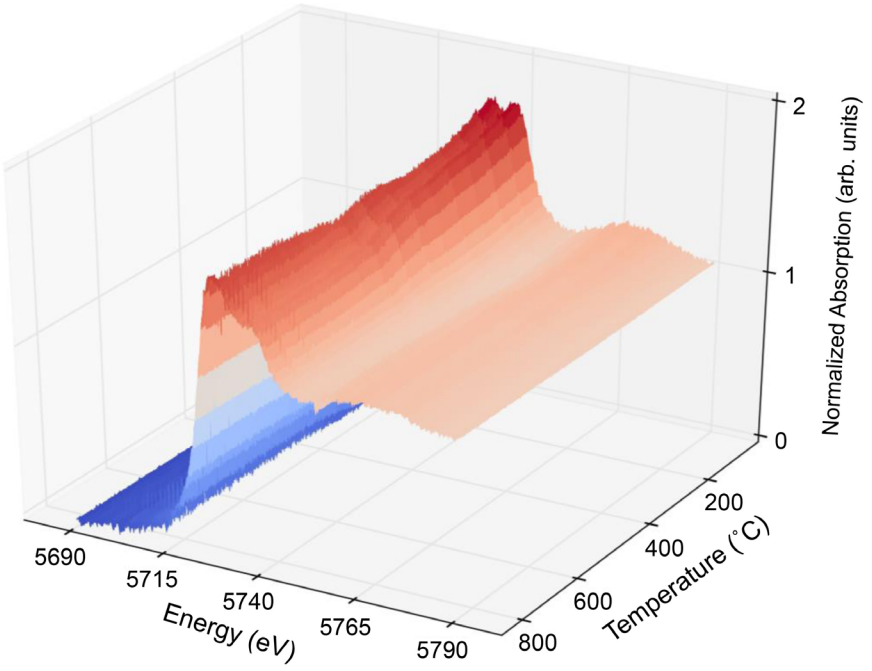

Figure 8. DXAS data at the Ce L_3-edge collected upon heating under 5 mol% H_2/He up to 600˚C for SDC nanopowder calcined at 400˚C.

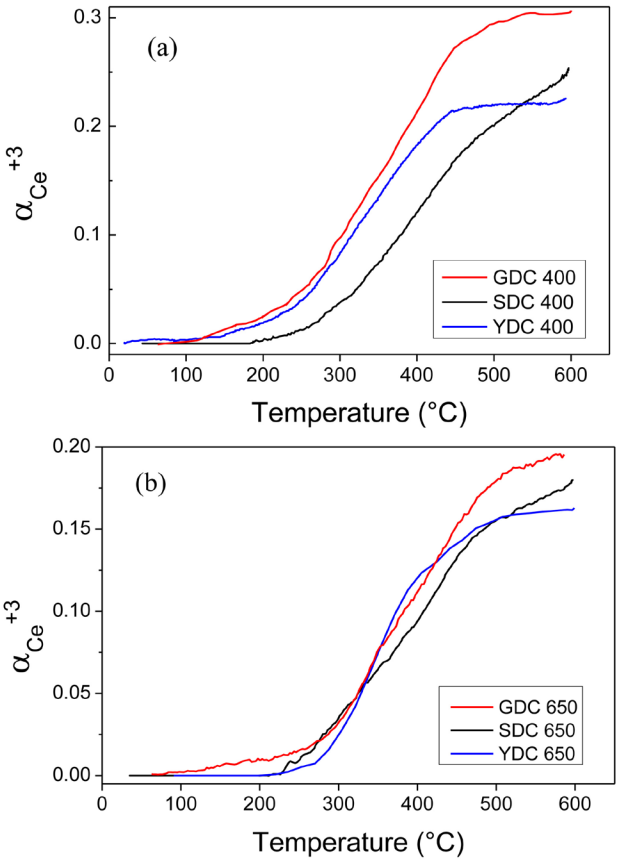

Figure 9. Ce^{3+} fraction (α_{Ce}^{3+}) for the GDC, SDC and YDC samples, treated at (a) 400˚C and (b) 650˚C, obtained from DXAS analysis.

GDC for both sets samples (calcined at 400˚C and 650˚C), clearly indicates its higher reducibility compared to SDC and YDC systems, in excellent agreement with TPR results.

4. Conclusions

In this work, we analyzed by the effect of average crystallite size and dopant oxide on the reducibility of CeO_2-based nanopowders by temperature-programmed reduction and dispersive X-ray absorption spectroscopy techniques.

We obtained samples formed by single-crystalline particles of controlled grain size, ranging between 4 to around 50 nm of diameter. The addition of Gd_2O_3 or Y_2O_3 has shown to inhibit grain growth more efficiently than Sm_2O_3.

Our results obtained from combined TPR and *in situ* DXAS, evidenced that:

- Gd_2O_3-doped ceria display better reducibility than Y_2O_3- and Sm_2O_3-doped ceria.
- Reducibility is enhanced in the samples formed by small sized crystallites.

Even though all the materials studied in this work exhibited good properties and, therefore, are likely to be used as anodes of intermediate-temperature SOFCs, Gd_2O_3-doped CeO_2 nanopowders presented the best performance and are more promising for applications.

Acknowledgements

The present work was partially supported by the Brazilian Synchrotron Light Laboratory (LNLS, Brazil, proposals DXAS-10900, XAFS1-13662 and XAFS1-15360), Agencia Nacional de Promoción Científica y Tecnológica (Argentina, PICT 2015 No. 3411 and PICT 2016 No. 1921) and CAPES-MinCyT bilateral cooperation. The authors thank Prof. Márcia Fantini for her help during X-ray powder diffraction and DXAS measurements and for her valuable comments.

Conflicts of Interest

The authors declare no conflicts of interest regarding the publication of this paper.

References

[1] Trovarelli, (1996) Catalytic Properties of Ceria and CeO_2-Containing Materials. *Catalysis Reviews*, **38**, 439-520. https://doi.org/10.1080/01614949608006464

[2] Kaspar, J., Fornasiero, P. and Graziani, M. (1999) Use of CeO_2-Based Oxides in the Three-Way Catalysis. *Catalysis Today*, **2**, 285-298. https://doi.org/10.1016/S0920-5861(98)00510-0

[3] Fu, Q., Weber, A. and Flytzani-Stephanopoulo, M. (2001) Nanostructured Au-CeO_2 Catalysts for Low-Temperature Water-Gas Shift. *Catalysis Letters*, **77**, 87-95. https://doi.org/10.1023/A:1012666128812

[4] Fu, Q., Saltsburg, H. and Flytzani-Stephanopoulo, M. (2003) Active Nonmetallic Au and Pt Species on Ceria-Based Water-Gas Shift Catalysts. *Science*, **301**, 935-938. https://doi.org/10.1126/science.1085721

[5] Beie, H.J. and Gnörich, A. (1991) Oxygen Gas Sensors Based on CeO_2 Thick and Thin Films. *Sensors and Actuators B*: *Chemical*, **4**, 393-399. https://doi.org/10.1016/0925-4005(91)80141-6

[6] Jasinski, P., Suzuki, T. and Anderson, H.U. (2003) Nanocrystalline Undoped Ceria Oxygen Sensor. *Sensors and Actuators B*: *Chemical*, **95**, 73-77. https://doi.org/10.1016/S0925-4005(03)00407-6

[7] Stoukides, M. (2000) Solid-Electrolyte Membrane Reactors: Current Experience and Future Outlook. *Catalysis Reviews*, **42**, 1-70. https://doi.org/10.1081/CR-100100259

[8] Yin, X., Hong, L. and Liu, Z.L. (2006) Oxygen Permeation through the LSCO-80/CeO_2 Asymmetric Tubular Membrane Reactor. *Journal of Membrane Science*, **268**, 2-12. https://doi.org/10.1016/j.memsci.2005.06.005

[9] Steele, C.H. (2000) Appraisal of $Ce_{1-y}Gd_yO_{2-y/2}$ Electrolytes for ITSOFC Operation at 500 ˚C. *Solid State Ionics*, **129**, 95-110. https://doi.org/10.1016/S0167-2738(99)00319-7

[10] Park, S.D., Vohs, J.M. and Gorte, R.J. (2000) Direct Oxidation of Hydrocarbons in a Solid Oxide Fuel Cells. *Nature*, **404**, 265-267. https://doi.org/10.1038/35005040

[11] Sun, W., Hui, R. and Roller, J. (2010) Cathode Materials for Solid Oxide Fuel Cells: A Review. *Journal of Solid State Electrochemistry*, **14**, 1125-1144. https://doi.org/10.1007/s10008-009-0932-0

[12] Sun, W. and Stimming, U. (2007) Recent Anode Advances in Solid Oxide Fuel Cells. *Journal of Power Sources*, **171**, 247-260. https://doi.org/10.1016/j.jpowsour.2007.06.086

[13] Tuller, H.L. (2000) Ionic Conduction in Nanocrystalline Materials. *Solid State Ionics*, **131**, 143-157. https://doi.org/10.1016/S0167-2738(00)00629-9

[14] Bellino, M.G., Lamas, D.G. and Walsöe de Reca, N.E. (2006) Enhanced Ionic Conductivity in Nanostructured, Heavily Doped Ceria Ceramics. *Advanced Functional Materials*, **16**, 107-113. https://doi.org/10.1002/adfm.200500186

[15] Zimicz, M.G., Larrondo, S.A., Prado, R.J. and Lamas, D.G. (2012) Time-Resolved *in Situ* XANES Study of the Redox Properties of $Ce_{0.9}Zr_{0.1}O_2$ Mixed Oxides. *International Journal of Hydrogen Energy*, **37**, 14881-14886. https://doi.org/10.1016/j.ijhydene.2012.01.162

[16] Zimicz, M.G., Prado, F.D., Soldati, A.L., Lamas, D.G. and Larrondo, S.A. (2015) XPD and XANES Studies of $Ce_{0.9}Zr_{0.1}O_2$ Nanocatalysts under Redox and Catalytic CH_4 Oxidation Conditions. *The Journal of Physical Chemistry C*, **119**, 19210-19217. https://doi.org/10.1021/acs.jpcc.5b05253

[17] Zimicz, M.G., Prado, F.D., Lamas, D.G. and Larrondo, S.A. (2017) *In-Situ* XANES and XPD Studies of NiO/$Ce_{0.9}Zr_{0.1}O_2$ IT-SOFCs Anode Nanomaterial as Catalyst in the CPOM Reaction. *Applied Catalysis A*: *General*, **542**, 296-305. https://doi.org/10.1016/j.apcata.2017.05.040

[18] Toscani, L.M., Zimicz, M.G., Martins, T.S., Lamas, D.G. and Larrondo, S.A. (2018) *In Situ* X-Ray Absorption Spectroscopy Study of CuO-NiO/CeO_2-ZrO_2 Oxides: Redox Characterization and Its Effect in Catalytic Performance for Partial Oxidation of Methane. *RSC Advances*, **8**, 12190-12203. https://doi.org/10.1039/C8RA01528G

[19] Bacani, R., Toscani, L.M., Martins, T.S., Fantini, M.C.A., Lamas, D.G. and Larrondo, S.A. (2017) Synthesis and Characterization of Mesoporous NiO_2/ZrO_2-CeO_2 Catalysts for Total Methane Conversion. *Ceramics International*, **43**, 7851-7860. https://doi.org/10.1016/j.ceramint.2017.03.101

[20] Chen, P.-L. and Chen, I.W. (1996) Grain Growth in CeO_2: Dopant Effects, Defect

Mechanism, and Solute Drag. *Journal of the American Ceramic Society*, **79**, 1793-1800. https://doi.org/10.1111/j.1151-2916.1996.tb07997.x

[21] Inaba, H., Nakajima, T. and Tagawa, H. (1998) Sintering Behaviors of Ceria and Gadolinia-Doped Ceria. *Solid State Ionics*, **106**, 263-268. https://doi.org/10.1016/S0167-2738(97)00496-7

[22] Kingery, W.D., Bowen, H.K. and Uhlmann, D.R. (1976) Introduction to Ceramics. 2nd Edition, John Wiley, New York, 456.